REVIEWS

Journal of Semiconductors
(2022) 43, 021301
doi: 10.1088/1674-4926/43/2/021301
JOS

Avalanche photodiodes on silicon photonics

Yuan Yuan, Bassem Tossoun, Zhihong Huang, Xiaoge Zeng, Geza Kurczveil, Marco Fiorentino, Di Liang†, and Raymond G. Beausoleil

Hewlett Packard Labs, Hewlett Packard Enterprise, Milpitas, CA 95035, USA

Abstract: Silicon photonics technology has drawn significant interest due to its potential for compact and high-performance photonic integrated circuits. The Ge- or III–V material-based avalanche photodiodes integrated on silicon photonics provide ideal high sensitivity optical receivers for telecommunication wavelengths. Herein, the last advances of monolithic and heterogeneous avalanche photodiodes on silicon are reviewed, including different device structures and semiconductor systems.

Key words: avalanche photodiode; silicon photonics; photonic integrated circuit

Citation: Y Yuan, B Tossoun, Z H Huang, X G Zeng, G Kurczveil, M Fiorentino, D Liang, and R G Beausoleil, Avalanche photodiodes on silicon photonics[J]. *J. Semicond.*, 2022, 43(2), 021301. http://doi.org/10.1088/1674-4926/43/2/021301

1. Introduction

Data traffic has grown tremendously over the past few decades due to emerging applications, such as virtual reality (VR), the internet of things (IoT), artificial intelligence (AI), and cloud computing. The rapid and unceasing growth of data communication leads to a strong demand for higher bandwidth. However, the ever-increasing data rate inside the data centers and high-performance computers (HPCs) has outstripped the capacity of traditional copper interconnects in terms of bandwidth, power efficiency, and crosstalk. Optical interconnects have been widely deployed for reach longer than a couple meters to alleviate the bottleneck of traditional copper wires due to their much larger bandwidth and negligible optical loss in present intra- and inter-data center applications. Recently, silicon photonics (SiPh) technology has drawn significant interest as a promising photonic integrated circuit (PIC) platform compatible to and benefited from the advanced complementary metal–oxide–semiconductor (CMOS) technology. Indeed, the economic benefits of high-volume manufacturing makes low-cost SiPh PICs appealing, thus promisingly cheap and high-performance optical interconnects. While SiPh is an ideal platform from many material and fabrication perspectives, the bandgap of silicon (Si), ~ 1.12 eV, leads to a transparent absorption window across telecommunication wavelengths of 1310 and 1550 nm, making silicon itself a poor optical receiver. The optical receiver (Rx) is an indispensable part of optical interconnects, a high-speed, high-sensitivity Rx can improve the performance of the whole link and reduce the requirements of other active and passive key components. Many works have been done to realize a high-performance photodiodes (PDs) on Si[1], including germanium (Ge) p–i–n PDs[2, 3], Ge traveling-wave PDs[4, 5], heterogeneously integrated III–V p–i–n and uni-traveling carrier (UTC) PDs[6, 7], heteroepitaxy III–V p–i–n and UTC PDs[8, 9], metal–semiconductor–metal (MSM) PDs[10, 11], and two-dimensional materials PDs[12, 13]. Compared to conventional PDs, avalanche photodiode (APD) exhibits a higher sensitivity due to its internal gain. The high electric field (E-field) inside the APD multiplication region accelerates the photon-generated carriers (electrons and holes) until they obtain sufficient energy to promote new electrons from the valance band into conduction band, creating new electron-hole pairs. This process is known as impact ionization, which leads to the amplified electric output signal from APDs. Accordingly, the internal amplification can improve the receiver signal-to-noise ratio (SNR) and help detect very weak optical signals[14]. The SNR of the APD can be expressed as

$$\mathrm{SNR} = \frac{I_{\mathrm{photo}}^2}{2qI_{\mathrm{total}}F(M)\Delta f + \dfrac{\sigma_{\mathrm{circuit}}^2}{M^2}}, \tag{1}$$

where I_{photo} is photocurrent, I_{total} is total current, q is elementary electric charge, $F(M)$ is excess noise factor, Δf is bandwidth, M is average gain, and $\sigma_{\mathrm{circuit}}^2$ is the root mean square (RMS) noise current of the following electronic circuitry. APD gain can effectively suppress the electronic circuit noise until the APD noise is equivalent to the circuit noise. In this work, we provide an overview on the recent research of APDs on Si, including monolithic and heterogeneous integrated APDs with different material systems. Numerous effort has been done to boost the bandwidth and sensitivity performance of Si-integrated APDs to make it an attractive Rx solution for next-generation optical interconnects.

2. Integrated APDs on silicon

To achieve efficient absorption at attractive near-infrared wavelengths, such as 1310 and 1550 nm, different semiconductor materials with narrower bandgaps have been integrated on Si. The integration of CMOS-compatible semiconductors, e.g., Ge, on a SiPh platform can easily leverage the mature CMOS technologies and provide high-performance photonic devices with low manufacturing costs. There is also no fundamental roadblock to prevent CMOS-incompatible

Correspondence to: D Liang, di.liang@hpe.com
Received 3 JULY 2021; Revised 3 SEPTEMBER 2021.
©2022 Chinese Institute of Electronics

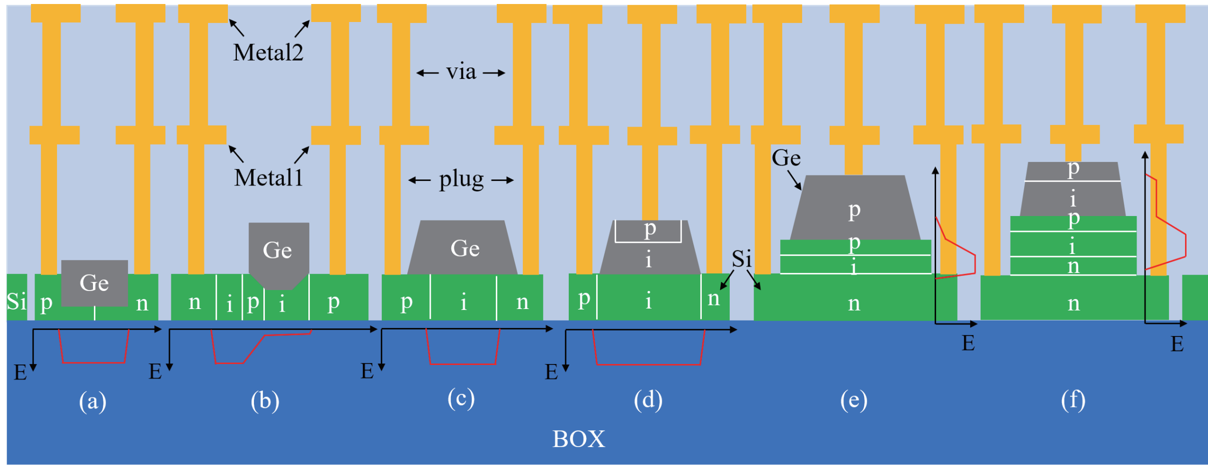

Fig. 1. (Color online) Common structures of Si–Ge APDs with E-field: (a) lateral p–i–n Si–Ge–Si APD[18], (b) Ge on lateral SACM Si APD[19], (c) Ge on lateral p–i–n Si APD[20], (d) hybrid vertical and lateral p–i–n APD[21], (e) vertical SACM p–p–i–n APD[22], and (f) vertical SACM p–i–p–i–n APD[23, 24].

materials, e.g., III–V, integrated on the large-scale Si wafers from being processed in a dedicated 200 or 300 mm process line to benefit process accuracy and throughput in CMOS production lines because of Intel's huge success to commercialize III–V-on-Si diode lasers in their 300 mm production lines. Several integration methods have been developed to achieve high quality semiconductors on Si, including monolithic and heterogenous integrations. In this section, we introduce several typical material systems for SiPh-integrated APDs, namely Si–Ge, III–V, and QD APDs.

2.1. Si–Ge APDs

Similar to Si, Ge is a group-IV crystalline semiconductor. It is a widely used complementary material for Si in both electronics and photonics circuits that can be directly grown on Si. For light detection, Ge is an excellent material as its ~ 0.8 eV bandgap is narrow enough for efficient absorption in telecommunication wavelength windows, and the fast mobility of electrons and holes provides potential for high speed. Although the 4.2% lattice mismatch between Ge and Si causes misfits and threading dislocations, the improved growth techniques can reduce the dark current of Si–Ge APDs to an acceptable level[15]. In the past ten years, with the development of SiPh, monolithic Si–Ge APDs have attracted extensive research interest. Si itself is a decent material candidate for the APD multiplication region because of its extremely low ratio of the impact ionization coefficients for holes and electrons, k, being only about 0.01–0.02 versus ~ 0.9 for Ge and ~ 0.4 for InP. For bulk multiplication regions, the excess noise factor $F(M)$ is a function of the average gain M and multiplication layer k value, which is given by[16]

$$F(M) = kM + (1 - k)(2 - 1/M). \tag{2}$$

The excess noise factor increases with increasing gain M, while increases slower with lower k value. A low k means that electrons are much easier to get impact ionization than holes, reducing the stochastic gain fluctuations, thus the source of the excess noise is suppressed. In addition, Emmons has shown that low k value is also helpful for high gain-bandwidth product (GBP) in Ref. [17]. Consequently, a multiplication region with low k value is desired in APD. Due to similar electron and hole ionization coefficients for Ge, its k value is close to unity (~ 0.9). Therefore, utilizing Ge as the absorption region and Si as the multiplication region can achieve advantages of both materials. Many device structures have been proposed for monolithic Si–Ge APDs, as shown in Fig. 1, from left to right, including lateral, hybrid vertical and lateral, and vertical structures.

Fig. 1(a) is a simple lateral p–i–n APD with a Si–Ge–Si heterojunction. The E-field at the Si–Ge interface is larger than that in the intrinsic Ge region, so that most impact ionization events occur at the interfaces of Si–Ge heterojunction and result in an effective k ~ 0.25[18]. Benedikovic *et al.* reported the lateral Si–Ge–Si waveguide APD at 1550 nm with a breakdown voltage of ~ –11 V, highest gain of ~120, responsivity of ~ 0.29 A/W, bandwidth of ~ 33 GHz, GBP of ~ 210 GHz, and open eye diagrams at 40 Gb/s NRZ that with sensitivity ~ –11.2 dBm for 10^{-9} bit error rate (BER) as shown in Fig. 2(a)[18]. Fig. 1(b) shows a lateral APD with separate absorption, charge, multiplication (SACM) regions. Due to the lateral p–i–p–i–n doping structure inside the Si, the E-field is concentrated on the left Si intrinsic region to be the multiplication region. And the absorption region, Ge, is grown into the cavity of the right Si intrinsic region to protect Ge from high E-field. The light will be coupled into the Ge layer and then absorbed, the photon-generated carriers then drift to the left Si regions and only get impact ionization inside the multiplication region. Srinivasan *et al.* proposed the lateral SACM Si–Ge APD at 1550 nm with a breakdown voltage of ~ –12 V, highest RF gain of ~ 11, responsivity of ~ 0.78 A/W, bandwidth of ~ 27 GHz, GBP of ~ 300 GHz, and open eye diagrams at 50 Gb/s NRZ as shown in Fig. 2(b)[19]. Differently, a lateral p–i–n Si APD with Ge on the top is shown in Fig. 1(c). The Ge absorption is directly grown on the top of the Si intrinsic region, since there is no charge layer, and the E-field will be distributed inside the intrinsic Ge and Si region. As a narrow bandgap semiconductor, Ge needs lower E-field to start impact ionization than Si, thus most carriers will be amplified inside the Ge and exhibit higher excess noise. Zhang *et al.* demonstrated the Ge on lateral Si p–i–n APD that exhibits an effective k of within 0.4–0.6, a breakdown voltage of ~ –12.5 V, a gain up to 16, a responsivity of ~ 0.95 A/W, a bandwidth up to 33 GHz, and detectable signals with 32 Gbaud PAM4 and 40 Gbaud 16QAM modulations at 1550 nm. The *I–V*

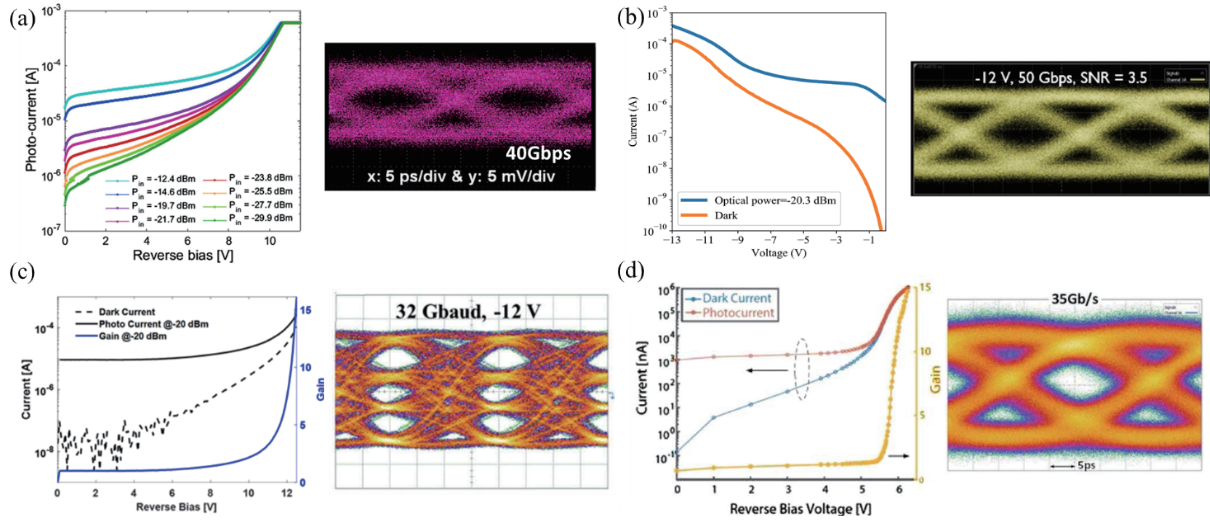

Fig. 2. (Color online) *I*–*V* curves and eye diagrams of (a) lateral p–i–n Si-Ge-Si APD[18], (b) Ge on lateral SACM Si APD[19], (c) Ge on lateral p–i–n Si APD[20], and (d) hybrid vertical and lateral p–i–n APD[21].

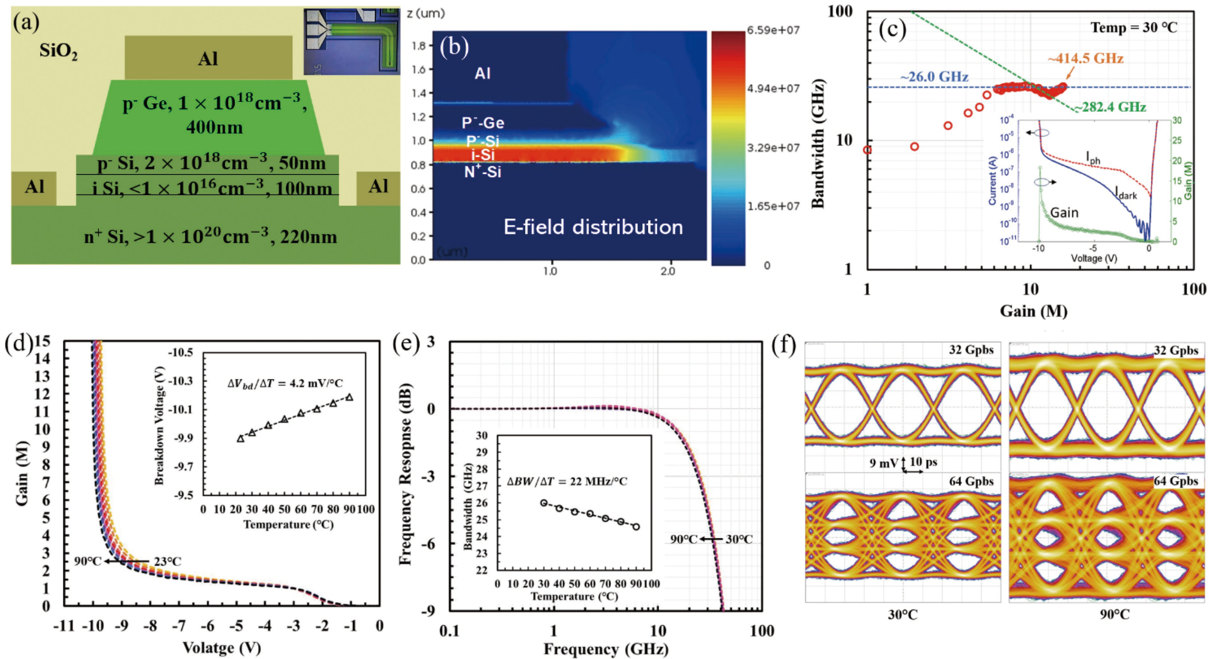

Fig. 3. (Color online) (a) A cross-sectional structure, (b) a simulated E-field distribution, (c) a gain vs bandwidth plot, temperature-dependent characteristics of (d) gain and breakdown voltage, (e) bandwidth, and (f) 32 Gb/s NRZ and 64 Gb/s PAM4 eye diagrams of the 4 × 10 μm^2 Si–Ge SACM APD[22, 28, 31].

curves and PAM4 eye diagrams are shown in Fig. 2(c)[20]. The hybrid vertical and lateral Si–Ge APD structure is shown in Fig. 1(d). Compared to Fig. 1(c), the main difference is the bias on Ge, it is a three-terminal device that allows individual E-field control in Ge and Si. The carriers are generated and transited in vertical structure, and then multiplied in a lateral Si structure. This structure can control all impact ionization events that occur inside Si for low excess noise. Fig. 2(d) shows the *I*–*V* and eye diagrams of the three-terminal Si–Ge APD demonstrated by Zeng *et al.* A benefit from the directly E-field control within the Si, the three-terminal APD enables a very low breakdown voltage of ~ –6 V, a responsivity of ~ 0.48 A/W, a bandwidth of ~ 19 GHz, and clear eye diagrams at 35 Gb/s NRZ at 1550 nm[21]. As for the common vertical structure, Figs. 1(e) and 1(f) illustrate the Si–Ge SACM APDs with p–p–i–n[22] and p–i–p–i–n[23, 24] structures, respectively. Both structures can ensure carriers get impact ionization in the Si multiplication region. Thanks to the fast diffusion velocity of Ge, the p–p–i–n SACM APD is also able to exhibit high bandwidth of ~ 25 GHz without being limited by carrier transit time[22].

In addition to concentrating the electric field to form the multiplication region inside low *k* value Si, the thickness of the multiplication region is also important. A thin multiplication region can reduce the carrier transit time, which is the premise of achieving high bandwidth. Besides that, the dead-space effect cannot be ignored. Unlike the excess noise local model of Eq. (2), a non-local model is necessary because the carrier history should be included for the thin multiplication region[25–27]. The effective *k* value will be further reduced with

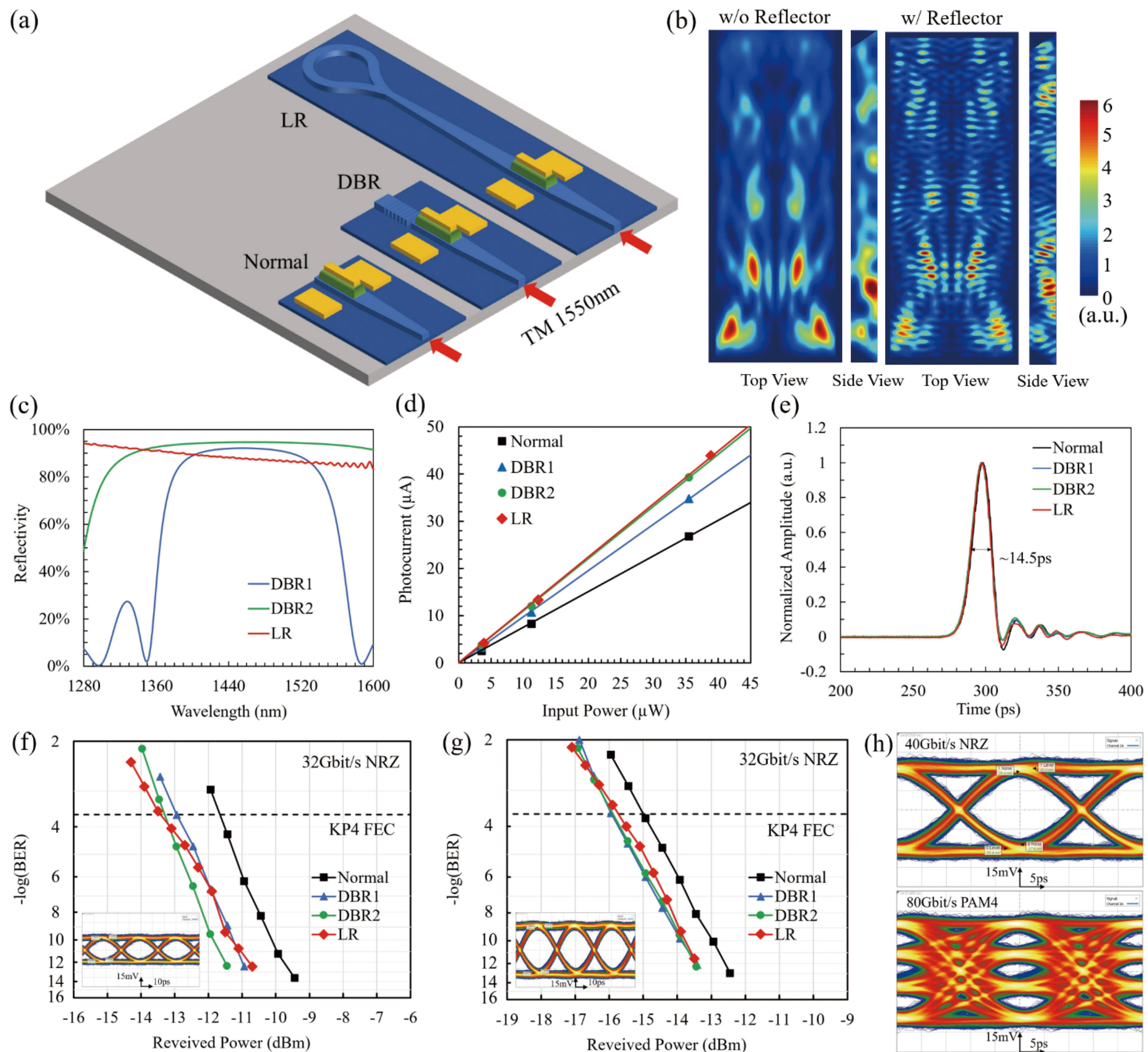

Fig. 4. (Color online) (a) Schematic of the Si–Ge APD with no reflector (Normal), a distributed Bragg reflector (DBR), and a loop reflector (LR), and (b) simulated absorption profiles. Comparison of (c) reflectivity, (d) photocurrent versus input power at unity gain point (e) impulse responses at gain ~ 10, 32 Gb/s NRZ bit error rate at bias voltage of (f) –8 V and (g) –10 V between the Normal, DBR1, DBR2, and LR APDs. (h) 40 Gb/s NRZ and 80 Gb/s PAM4 eye diagrams of the LR APD at bias of –10 V[32, 33].

the dead-space effect. In the Hewlett Packard Enterprise (HPE), we demonstrated the Si–Ge waveguide SACM APDs with a p–p–i–n structure, as shown in Figs. 3(a) and 3(b), a 100 nm-thick intrinsic Si is used as the multiplication region and the E-field is confined inside it[22]. This thin Si multiplication layer enables a high bandwidth and GBP because of the small transit time and build-up time. At 30 °C, the 4 × 10 μm^2 Si–Ge waveguide APD exhibits a 3-dB bandwidth of ~ 26 GHz and a GBP of ~ 282.4 GHz as shown in Fig. 3(c)[28]. And the inset *I–V* curve shows the Si–Ge APD has a low breakdown voltage of ~ –10 V with a highest gain ~ 20. All the measurements for the Si–Ge SACM APD are based on a 1550 nm laser. Another benefit of the thin multiplication region is its great thermal stability. The thin multiplication region requires a higher E-field to achieve the same gain than the thick one, such that carriers obtain sufficient ionization energy more quickly, and it results in less phonon scattering before avalanche breakdown. Therefore, carriers are less sensitive to temperature-dependent phonon energy[29, 30]. Figs. 3(d)–3(f) illustrate the temperature-dependent characteristics of gain, bandwidth, and eye diagrams, respectively[31]. The 100 nm multiplication region Si–Ge SACM APD exhibits an excellent temperature stability as the breakdown voltage only increases ~ 4.2 mV/°C, bandwidth only reduces ~ 22 MHz/°C, and clear eye diagrams with 32 Gb/s NRZ and 64 Gb/s PAM4 are obvious at both 30 and 90 °C.

The 4 × 10 μm^2 Si–Ge SACM APD has shown high-speed performance because the waveguide SACM structure decouples the photon absorption length (10 μm) in the wafer plane and carrier transit length (100 nm) normal to the wafer plane. However, there is still a trade-off between absorption length and RC time constant. To further loosen the trade-off, different simple Si mirrors have been integrated at the end of the Si–Ge waveguide APD to improve its responsivity without compromising the bandwidth[32, 33]. Fig. 4(a) shows the schematic of the Si–Ge APD with no reflector (Normal), a distributed Bragg reflector (DBR), and a loop reflector (LR). The integrated DBR and LR reflect the unabsorbed light after the first

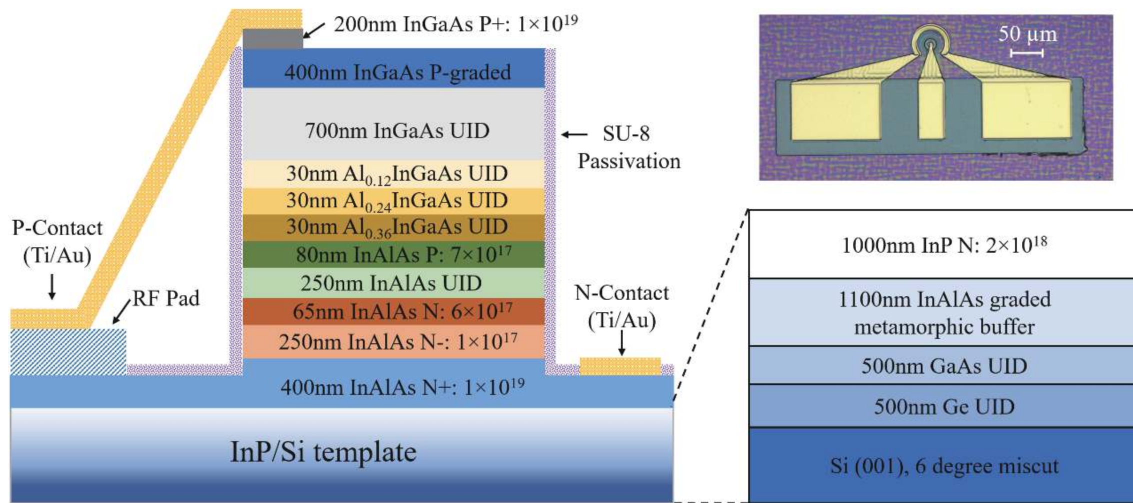

Fig. 5. (Color online) Cross-sectional schematic of the InGaAs/InAlAs SACM APD directly on the InP/Si template[52].

pass back into the APD forming a dual-path absorption. The simulated absorption profiles for the APD without and with a reflector are shown in Fig. 4(b), where the reflected light interferes with the incident light to cause the interference fringes for the APD with reflector. We have demonstrated three reflector designs, including DBR1 with 267 nm groove and 428 nm teeth, DBR 2 with 211 nm groove and 173 nm teeth, both 5 μm wide, and LR with 500 nm waveguide width and 10 μm loop radius. Comparison of the calculated reflectivity for these three reflectors is illustrated in Fig. 4(c), they all have considerable reflectivity > 70% at 1550 nm. The measured photocurrent versus input optical power at the unity gain point is shown in Fig. 4(d), the extracted responsivity of the Normal APD is ~0.75 A/W and it is improved up to ~0.98, 1.10, and 1.12 A/W for DBR1, DBR2, and LR APDs, respectively. The enhanced responsivity is not only caused by the dual-path absorption but also the light interference. The interference between reflected and incident light changes the mode oscillation between the Si and Ge layers, it also creates a better absorption profile. The speed performance of Normal, DBR1, DBR2, and LR APDs can be evaluated by their impulse responses as displayed in Fig. 4(e), where a femtosecond 1550 nm laser was used as the source. The full width at half maximum (FWHM) of the impulse responses are all around 14.5 ps, which indicates that all four APDs have similar speed performance. Adding a reflector does not delay the overall response process of APDs.

The enhanced responsivity can further improve the sensitivity of the low noise Si–Ge APDs. Figs. 4(f) and 4(g) show the comparison of their BERs at bias voltage of –8 and –10 V, respectively. A 32 Gb/s bit error rate tester was used to measure the BERs with 32 Gb/s NRZ operation. The BER of error-free transmission with KP4 forward error correction (FEC) is 2.4×10^{-4} as dash lines indicate in Figs. 4(f) and 4(g). At the bias of –8 V, Normal, DBR1, DBR2, and LR APDs achieve a sensitivity of ~ 11.7, –12.9, –13.3, and –13.4 dBm, respectively. The reflector-assisted APDs achieve 1–2 dB better sensitivity. Increasing the bias voltage to –10 V, Normal, DBR1, DBR2, and LR APDs obtain sensitivity of –15.0, –16.0, –15.9, and –15.7 dBm, respectively. And the APDs with reflector still allow ~ 1 dB better sensitivity. The high sensitivity Rx is desired in optical links, which can reduce the laser source power consumption and improve overall link energy efficiency. The Si–Ge waveguide APD with p–p–i–n SACM structure has been proved to have low excess noise, low operation voltage, high speed, high sensitivity, and excellent temperature stability characteristics. By adding the reflector at the end of the APD waveguide, the sensitivity can be further improved without changing any speed performance. We believe the high-performance Si–Ge SACM APD is an attractive Rx for future sub-pJ/bit optical links.

2.2. III–V APDs grown directly on silicon

III–V compound semiconductors have been widely used in active photonics devices due to their direct bandgaps, variable band structures, and flexible complex structure design. Integration of III–V semiconductors on Si has attracted significant interest as it can provide high-performance III–V photonics devices on SiPh platform, especially for lasers[34–36]. At telecommunication wavelengths, conventional III–V APDs, such as InGaAs/InAlAs and InGaAs/InP SACM APDs, have shown low dark current, low excess noise, high bandwidth, and high GBP performance[37–40]. In addition to being the ideal candidate Rx in optical interconnects, the low dark current III–V APDs also show a potential for single-photon detection[41–43]. Integrating III–V APDs with SiPh PICs can improve performance, reduce cost, and expand applications, such as light detection and ranging (LiDAR)[44–46] and quantum photonic circuits[47, 48]. Several approaches have been demonstrated to integrated III–V materials on Si, for example hybrid integration through packaging, and heterogeneous integration through wafer bonding or transfer printing[36, 49, 50]. In this section, we focus on integrating III–V APDs on Si by heteroepitaxy[51]. The first III–V APD grown directly on Si is reported in Ref. [52]. The InGaAs/InAlAs SACM APDs have been chosen to grow on a InP/Si template, whose cross-sectional schematic is shown in Fig. 5, where InGaAs is used as p-type contact and absorption layers, $Al_xInGaAs$ is used as band structure grading layers, InAlAs is used as charge, multiplication, buffer, and n-type contact layers. The APD sample was grown on a InP/Si template at 500 °C after 10 min oxide desorption on the InP surface with As_2 overpressure[52]. The InP/Si template, from top to bottom, is composed of InP, InAlAs, GaAs, Ge, and Si layers as shown in Fig. 5.

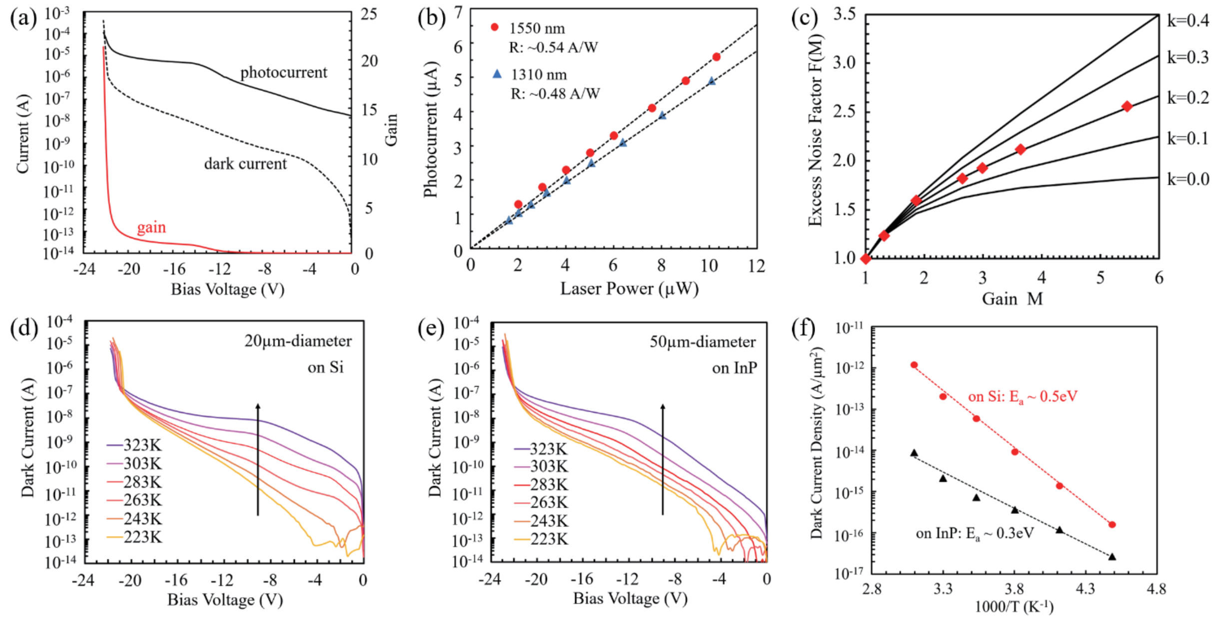

Fig. 6. (Color online) (a) I–V and gain curves, (b) photocurrent versus input laser power at unity gain point, and (c) excess noise of the 20 μm-diameter InGaAs/InAlAs APD on Si. Temperature-dependent dark current versus bias voltage of the (d) 20 μm-diameter APD on Si and (e) 50 μm-diameter APD on InP. (f) Activation energies at –5 V for APDs on Si and InP[52].

The characteristics of the InGaAs/InAlAs SACM APD on Si are illustrated in Fig. 6. The I–V and gain curves of the APD on Si was measured at 1550 nm, the punch-through voltage is ~ –14 V and the highest gain is up to ~ 20. As shown in Fig. 6(b), the unity gain point responsivity of the top illuminated APD was measured with 1550 and 1310 nm light, where the captured responsivity is ~ 0.54 and 0.48 A/W, respectively. Considering the different wavelength photon energies, the corresponding external quantum efficiency is ~ 43% at 1550 nm and ~ 46 % at 1310 nm. Fig. 6(c) shows the excess noise performance, the k value of the III–V APD on Si is ~ 0.2. It is consistent with the reported value of the InP-based APD with comparable thick InAlAs multiplication region[53]. One primary challenge of the heteroepitaxial method is the large lattice mismatch between III–V and Si, although Ge, GaAs and InAlAs layers all serve as a buffer for the InP/Si template, the concomitant defects in grown semiconductors are still inevitable where the defect density is ~ 10^8 cm^{-2}. The defect problem is particularly important for APD since it is a high E-field device. Therefore, another InGaAs/InAlAs APD on the InP substrate with the same epitaxial layers was grown for direct comparison. Figs. 6(d) and 6(e) show the temperature dependent dark current for a 20 μm-diameter APD on Si and a 50 μm-diameter APD on InP, respectively. The main difference is that the APD on Si has weaker temperature dependence of dark current at high voltages, which means the temperature-independent trap-assisted tunneling starts to dominate the dark current. The temperature variation of the dark current also indicates the thermal activation energy of the APDs,

$$I_{\text{dark}} \propto T^2 \exp\left(-\frac{E_a}{k_B T}\right), \tag{3}$$

where T is the absolute temperature, E_a is the activation energy, and k_B is the Boltzmann constant. At low bias voltage, the generation-recombination is the dominate dark current mechanism. The dark current density at bias voltage of –5 V is plotted in Fig. 6(f), the APD on Si exhibits 1–2 order higher dark current density than the one on InP. The activation energies then can be extracted, E_a is ~ 0.5 eV for the APD on Si while it is ~ 0.3 eV for the APD on InP, which implies that the APD on Si has a deeper generation-recombination defect center. In summary, the InGaAs/InAlAs SACM APD on Si by heteroepitaxy enables a high gain and a relatively high responsivity. It has as low excess noise as the APD on Si, however, the dark current is still higher due to the large lattice mismatch.

2.3. III–V quantum dot APDs on silicon

While Ge on Si APDs and III–V on Si APDs have proved to be efficient detectors in silicon-based photonic integrated circuits for data communications, one of the main issues with these devices is their relatively high dark currents, which increases noise and limits sensitivity at high data rates. For example, dark current densities of 5 A/cm^2 were measured for Ge-on-Si photodiodes operating at 1300 nm[54], 2 mA/cm^2 for a Ge-on-Si photodiode operating at 1550 nm[55, 53], and 1 mA/cm^2 for a monolithically integrated III–V on Si photodiode. One promising alternative for ultra-low dark current photodiodes on silicon is the III–V quantum dot (QD) photodiode integrated on silicon. Due to the three-dimensional confinement of carriers within quantum dots, these devices naturally have ultra-low dark currents[56]. Moreover, the high defect tolerance of QDs due to the strong localization of charges minimize the impact of dislocations within the QD absorption layers and keep the dark current low. Next, we will review recent progress of III–V QD APDs heterogeneously and monolithically integrated on Si.

2.3.1. Heterogeneously integrated III–V quantum dot APDs on silicon

Since there is a large lattice constant mismatch between Si (a_0 = 5.4310 Å) and most III–V compound semiconductors such as GaAs (a_0 = 5.6533 Å), InP (a_0 = 5.8687 Å) and InAs

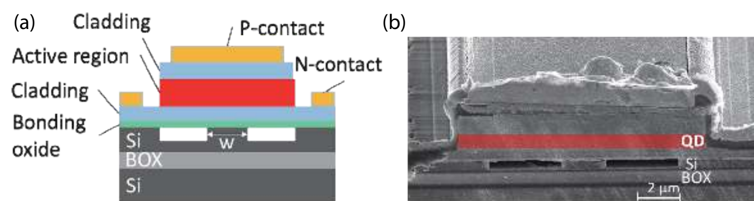

Fig. 7. (Color online) (a) Cross-section schematic of the photodiode. (b) SEM cross section of the QD waveguide PD on Si[59].

(a_0 = 6.0584 Å), and mismatches in polarity and thermal expansion coefficients, directly growing these types of materials on silicon would create a large number of dislocations, significantly degrading the performance and increasing the dark current of photodiodes fabricated out of these materials, as discussed above. Thick buffer layers or other dislocation filtering or blocking techniques have been helpful to reduce the dislocation density down to ~10^6 cm^{-3}, which is still a few orders of magnitude higher than the intrinsic value of epitaxial structures grow on a III–V native substrate. Thick buffer layers also prevent straightforward evanescent optical coupling between Si and III–V active region, which subsequently limits design flexibility of these devices in their integration with a silicon photonic integrated circuit. Heterogeneous integration offers the most practical and promising approach in the near-term to integrating high-performance III–V photonic devices directly onto silicon. This approach was discovered by Fang *et al.* in 2006 and since it has been developed and advanced significantly as a key technology for high-volume, low-cost on-chip active photonics, including photodetectors[57]. By growing the device epitaxial layers on a separate III–V substrate, and then bonding the III–V layers to silicon, one can fabricate high-performance devices made out of quality materials and prevent the dislocations produced by growing III–V layers directly onto silicon. Companies like Intel, Juniper Networks, and HPE have adopted this approach in order to develop low-cost on-chip lasers and photodetectors since[58].

In particular, HPE has used this method to fabricate InAs QD avalanche photodiodes heterogeneously integrated on silicon[59, 60]. The devices were notably made from the same epitaxial layers and fabrication process as QD comb lasers designed for dense wavelength-division multiplexing (DWDM) links. It shows the integration capability of these devices on a quantum dot-based silicon photonics platform. Fig. 7 shows a cross-section schematic of the quantum dot APD. The device consists of a p–i–n structure, in which the absorption region consists of eight layers of InAs quantum dots separated by 40 nm GaAs spacer layers, totaling 320 nm. The quantum dots were grown on a GaAs substrate using self-assembled growth in a molecular beam epitaxy (MBE) system[62]. The absorption coefficient of the entire QD active region was measured to be about 900 cm^{-1}. The intrinsic region of the p–i–n photo diode acts simultaneously as the absorption and multiplication layer of the APD. The III–V epitaxial material was bonded directly onto a silicon-on-insulator (SOI) wafer using an O_2 plasma-assisted wafer bonding process[63]. 320 nm thick ridge waveguides and grating couplers were etched directly on the SOI substrate, with a 1000 nm layer of buried oxide, before bonding. Next, mesas of different sizes were formed using a combination of dry and wet etching, and metals were deposited on p and n contacts and connected to RF pads for high-speed electrical measurements. The full fabrication process can be found in Ref. [59].

These APDs have shown the lowest dark current for any photodiode on silicon, as low as 10 pA (1 × 10^{-6} A/cm^2) at –1 V for a 11 × 30 μm^2 waveguide APD. Furthermore, the dark current density for a 11 × 60 μm^2 device was 2.7 × 10^{-6} A/cm^2 at –1 V and 3.4 × 10^{-6} A/cm^2 at –1 V for a 11 × 90 μm^2 device. The dark current scaling linearly with area suggests that the main contribution to the dark current comes from the bulk layers of the device. The low dark current is due to the combination of the 3-D carrier confinement of the QDs, good surface passivation of the PDs, low dislocation density and the high crystal quality of the active device material. Keeping the dark current low helps reduce the noise of the APD. The dark current was also measured as a function of temperature, as seen in Fig. 8(a). The breakdown voltage increases with temperature, implying that impact ionization is the main carrier mechanism behind the device breakdown.

Device testing starts from light coming from an O-band tunable laser which was coupled into the grating coupler and the silicon waveguide then evanescently coupled into the APD. The spectral response in the O-band was taken for an 11 × 90 μm^2 device and plotted in Fig. 8(b). There is both a wavelength and a bias dependence observed in the responsivity and gain of the device. This is accounted for by a combination of the avalanche gain and absorption of carriers within the device. As the wavelength of the input photons varies, the energy level of the photogenerated carriers within the QDs also varies. As carriers fill up the different energy levels, the carrier escape rates from the QDs change, altering the quantum efficiency, as well as the impact ionization rate of the carriers.

The responsivity at unity gain (–4 V) was 0.9 A/W at 1280 nm and 0.15 A/W at 1310 nm, implying a wavelength dependence on the absorption coefficient. At shorter wavelengths of the input optical mode, carriers are generated in the excited state within the QDs, and therefore, need less energy in order to escape the QDs. With the same bias voltage applied and an incoming 1310 nm optical signal, more carriers are generated in the ground state of the QD that need more energy in order to escape, causing a small amount of photocurrent being collected. Moreover, as the bias voltage increases, the absorption coefficient also shifts due to the quantum confined Stark effect (QCSE). The electron and hole wavefunctions inside the QDs shift with an increased in electric field applied, causing a subsequent shift in the absorption coefficient with wavelength[64].

The avalanche gain was measured and is shown in Fig. 8(c). With an input TE optical mode, a maximum gain of around 150 was measured at around –17.8 V, which is near the breakdown voltage. The polarization of the optical signal

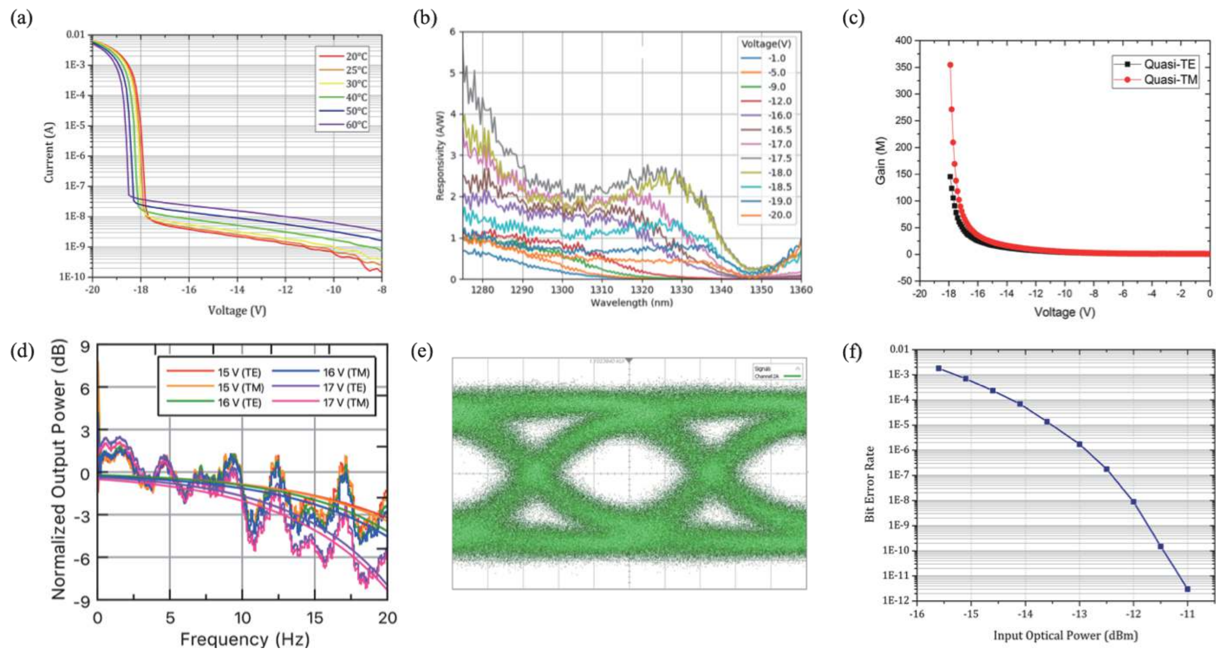

Fig. 8. (Color online) (a) Dark current vs. temperature for a 11 × 60 μm^2 APD. (b) Spectral response versus voltage of a 11 × 90 μm^2 APD. (c) Gain with quasi-TE mode and quasi-TM mode coupled into a 12 × 150 μm^2 APD. (d) Output frequency response of a 3 × 30 μm^2 APD measured with TE and TM modes at −15, −16 and −17 V bias voltage (dashed lines are averaged data). (e) Eye diagram of a 3 × 30 μm^2 APD with a gain of 46.8 at 25 Gb/s. (f) Bit error rate vs. input optical power of an 11 × 90 μm^2 APD at a gain of 28 at 10 Gbit/s[59].

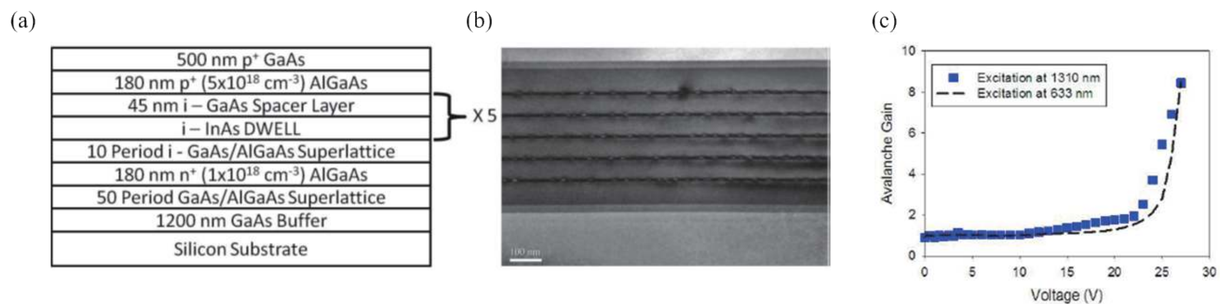

Fig. 9. (Color online) (a) Schematic of wafer structure. (b) TEM image of the wafer[67].

was then altered using a polarizer to change the input optical mode to the APD between TE and TM, and a polarization dependence on responsivity and gain was observed. With an input TM polarization, the gain increased by about a factor of 2 and the responsivity increased by a factor of 6. This is suggested to be due to a higher number of light holes being generated with TM polarization and then impact ionizing[65].

The high-speed dynamics was measured at −15, −16, and −17 V and can be seen in Fig. 8(d). These devices have also demonstrated a maximum 3-dB bandwidth of 20 GHz at and a maximum gain–bandwidth product (GBP) of 585 GHz, which is the record for III–V quantum dot APDs on silicon. 25 Gb/s open eye diagrams were also recorded (Fig. 8(e)) and a sensitivity of −11 dBm was measured at 10 Gb/s (Fig. 8(f)). Conclusively, III–V QD APDs heterogeneously integrated on silicon are still in their early stage of development but have a promising future as receivers in future WDM silicon photonic integrated circuits.

2.3.2. III–V quantum dot APDs monolithically grown on silicon

While wafer bonding has been successful in the development of high-performance III–V QD APDs on silicon, another promising approach is by monolithically growing III–V QD materials directly on silicon. The main advantages of this solution include ease of integration and scalability in regard to producing a large volume of devices on wafer. Also, due to the high defect sensitivity of QDs, the device performance will not be significantly reduced by dislocations. One way of growing III–V QD materials monolithically on Si is by using MBE and thick buffer layers. Another approach to this is by using metal organic chemical vapor deposition (MOCVD) and aspect ratio trapping. This method allows for the growth of GaAs on Si with a low defect density to produce QD avalanche photodiodes with low dark currents. Recently, there has been significant progress made on monolithically integrated QD APDs on silicon, which we discuss next.

The first InAs/GaAs QD photodetector monolithically integrated on silicon substrates was done using molecular beam epitaxy (MBE) by Wu *et al.*[66]. This device was grown directly on silicon using a GaAs buffer, reducing the threading dislocation density to ~10^6 cm^{-2}. Sandall *et al.* performed a study p–i–n photodiodes utilizing five periods of InAs/InGaAs dot-in-a-well (DWELL) grown on silicon substrates using MBE for absorption at around 1300 nm[67]. The device epitaxial layer

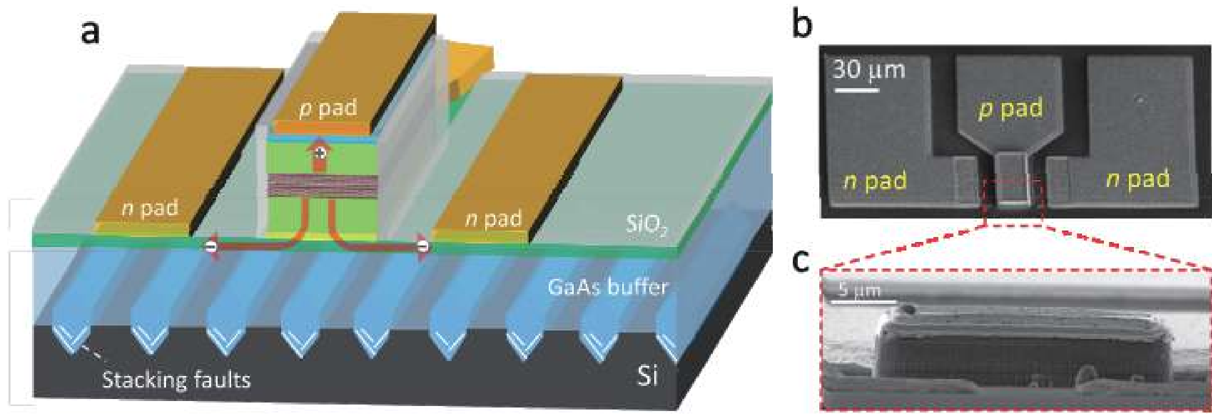

Fig. 10. (Color online) (a) Schematic plot of the PD fabricated on the GoVS template. (b) Top-view and (c) cross-sectional view SEM images of a fabricated device[68].

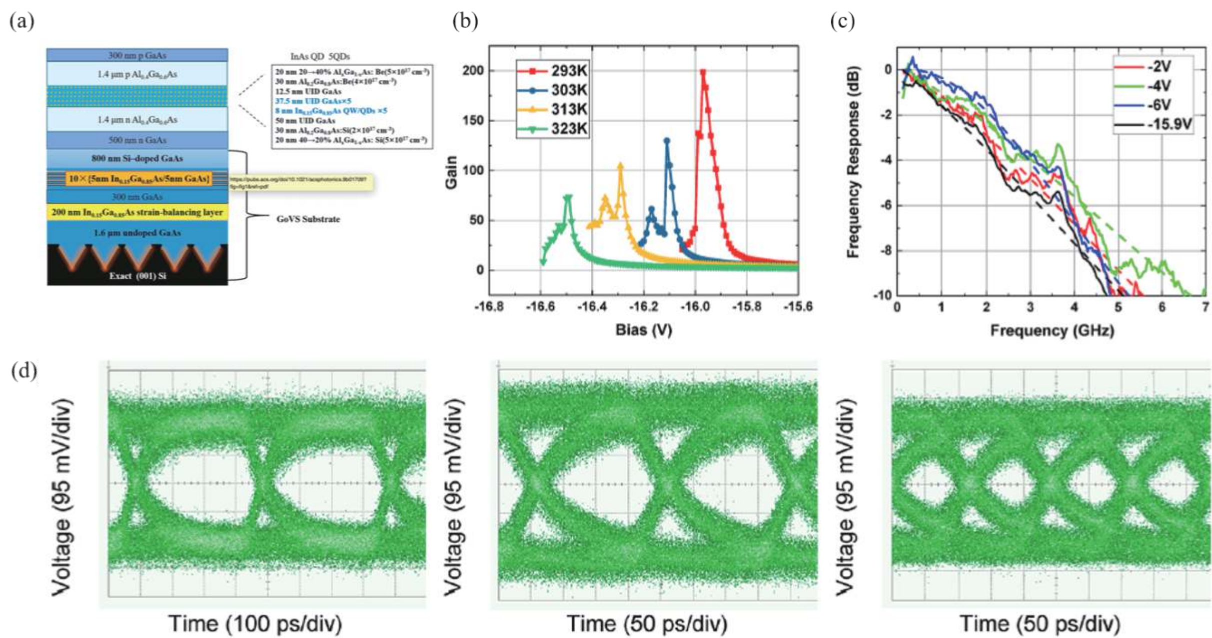

Fig. 11. (Color online) (a) Schematic diagram of the InAs QD APD grown on GoVS substrate. (b) APD gain versus the reverse bias at various temperatures. (c) Small-signal frequency response of the 3 × 50 μm^2 device for various bias voltages. (d) Measured eye diagrams at a bias voltage of −15.9 V for data rates of 2.5, 5, and 8 Gb/s[69].

structure as well as a TEM image of the wafer can be found in Figs. 9(a) and 9(b). The dark current density was measured to be in the range of 10^{-6} A/cm^2 for a 25 μm diameter circular mesa photodiode, which agrees with ultra-low dark current density observed in previously discussed heterogeneous counterparts. An avalanche gain as high as 8.5 was measured at about –26 V (Fig. 9(c)). Impact ionization was confirmed to be the main source of avalanche gain, and it was suggested that absorption occurs in the dot layers and the impact ionization events occur in the other layers of the depletion region. A peak responsivity of 5 mA/W was observed at 1280 nm for a 200 μm diameter circular mesa photodiode, and spectral response measurements indicate that the photon absorption in the QD layers is affected by the QCSE[67].

Wan *et al.* fabricated p–i–n photodetectors from InAs/GaAs QDs directly grown on a GaAs-on-V-grooved-Si (GoVS)[68]. The p–i–n structure included seven stacks of InAs DWELL structures with a dot density of 6 x 10^{10} cm^{-2}. A schematic plot, as well as top and cross-sectional views of the PD, can be seen in Fig. 10. First demonstrations of these devices showed a dark current as low as 0.8 nA, an internal responsivity of 0.9 A/W at 1250 nm, and a 3-dB bandwidth of 1.5 GHz measured and at a reverse bias voltage of –4 V. The high-frequency O/E response was limited by the combination of the RC time and hole escape time in the QDs, which was calculated to be about 30 ps.

Chen *at al.* measured device characteristics of InAs QD APDs grown with the same approach as Wan *et al.*[69]. These devices consisted of five layers of InAs QDs within a p–i–n structure. A schematic diagram of these devices can be found in Fig. 11(a). These APDs exhibited impressively low dark current at about 0.1 nA and a dark current density of 6.6 × 10^{-5} A/cm^2 at 300 K under a bias voltage of – 5 V. The gain was measured to be as high as 198 at 293 K (Fig. 11(b)). Furthermore, these devices showed an external responsivity as high as 0.234 A/W at 1310 nm and at unity gain (–5 V), and a 3-dB bandwidth of about 2.26 GHz at –6 V and 2.06 GHz at –16 V (Fig. 11(c)). The 3-dB bandwidth was limited by a combina-

Table 1. Properties of integrated APDs on silicon.

Ref.	Material	Structure	λ (nm)	V_{br} (V)	M	I_{dark} (nA)	R (A/W)	BW (GHz)	GBP (GHz)	BR (Gbps)
[21]	Si–Ge	Vertical + lateral p–i–n	1550	–6	15	1	0.48	19	/	NRZ 35
[18]	Si–Ge	Lateral p–i–n	1550	–11	120	47	0.29	33	210	NRZ 40
[19]	Si–Ge	Lateral SACM	1550	–12	11	10	0.78	27	300	NRZ 50
[32]	Si–Ge	Vertical SACM	1550	–10	24	20	1.12	25	296	PAM4 64
[20]	Si–Ge	Lateral p–i–n	1550	–12.5	16	10	0.95	33	/	PAM4 64
[70]	InGaAs	Vertical SAM	1310	–30	200	6	0.64	1.45	290	/
[52]	InGaAs–InAlAs	Vertical SACM	1550	–22	20	9	0.54	/	/	/
[67]	InAs–GaAs QD	Vertical p–i–n	1300	–26	8.5	0.8	0.005	/	/	/
[71]	InAs QD	Vertical p–i–n	1550	–23	12	0.01	0.48	/	/	/
[68]	InAs–InGaAs QD	Vertical p–i–n	1310	–16	/	0.8	0.13	1.5	/	/
[59]	InAs QD	Vertical p–i–n	1310	–19	45	0.1	0.34	15	240	NRZ 12.5
[69]	InAs QD	Vertical p–i–n	1310	–16	198	0.1	0.234	2.26	/	NRZ 8
[61]	InAs QD	Vertical p–i–n	1310	–19	350	0.01	0.15	20	585	NRZ 32

tion of the RC and transit time of the device. Furthermore, the transit time consists of both the carrier transport and carrier emission time out of the quantum dots. As the voltage increases into the high-gain regime of the APD, the bandwidth becomes limited by the avalanche buildup time. Open eye diagrams were shown for these devices as high as 8 Gb/s at a high gain bias point of –15.9 V, and can be seen in Fig. 11(d).

While growth of these materials directly on silicon is being developed, APDs made from these materials are not quite ready for practical usage within industry for mass volume production. Some of the challenges consist of a limited understanding of the growth mechanics and physical carrier mechanisms of quantum dot lasers and photodetectors. And while offering plenty of advantages on a device level, we still need a better understanding of how to mitigate issues such as lifetime, repeatability, temperature sensitivity, and design flexibility. However, in the long term, this integration approach may likely be the preferred method of growth for quantum dot avalanche photodiodes on a silicon photonics platform for high-speed optical interconnects for data communication within data centers and HPC systems.

2.4. Comparison of APDs on silicon

Properties of different material APDs integrated on Si are summarized in chronological order as shown in Table 1. It includes Si–Ge, InGaAs-InAlAs, InAs QD, InAs-GaAs QD, and InAs-InGaAs QD material systems; where λ is the working wavelength, V_{br} is the breakdown voltage, M is the highest gain, I_{dark} is the dark current at unity gain, R is the responsivity at unity gain, BW is the highest bandwidth, GBP is the gain-bandwidth product, and BR is bit rate of eye diagrams.

Si–Ge APD is the most popular APD on SiPh platform due to the maturity of Ge growth technology on Si. Table 1 shows five different structures of Si–Ge APDs. The thin multiplication region of these Si–Ge APDs enables low breakdown voltage and high bandwidth. Besides that, the extremely low excess noise of Si makes Si–Ge APDs suitable for high bit rate operations. In contrast to Ge, most III–V semiconductors have much bigger lattice mismatch with Si. Therefore, a lot of effort has been put into heterogeneous or monolithic III–V on Si integration. For example, the bulk InGaAs–InAlAs material system have monolithically grown on Si to form SACM APDs. Although, several buffer layers are added to reduce the large lattice mismatch, the InGaAs-InAlAs APD on Si still shows much higher dark current than the same APD grown on InP. To alleviate the high dark current problem, QD is a promising material system for III–V APDs on Si. QD materials have a higher defect tolerance as a result of the strong localization of charges, which is particularly effective for the high dislocations problem in III–V on Si integration. In addition, QD itself has low dark current property due to the nature of three-dimensional confinement. As shown in Table 1, InAs QD, InAs-GaAs QD, and InAs-InGaAs QD APDs have been integrated on Si heterogeneously or monolithically. All of these QD APDs have much lower dark currents at unity gain compared to Si–Ge and bulk III–V APDs. However, QD APDs on Si still have some drawbacks that need to be improved. First, most integrated QD materials on Si have a relatively wide bandgap, resulting in a weak edge absorption around 1310 nm. Also due to the QCSE, the edge absorption coefficient changes with the electric field. Most current QD APDs on Si have a vertical p–i–n structure, such that light is absorbed and multiplicated in the same QD layer. It leads to high excess noise and a tighter trade-off between bandwidth and responsivity, which limits the high data rate performance.

Although the above material systems have been successfully monolithic or heterogeneous integrated on Si, APDs based on these materials still face challenges. For Si–Ge APDs, the dark current is still relatively high due to the lattice mismatch between Si and Ge. By further reducing misfits and threading dislocations at the Si–Ge interface, a dark current can be suppressed and thus enables better sensitivity. A similar problem of high dark current also exists for bulk III–V APDs on Si, requiring more efficient buffer layers to relive the stress between III–V and Si. Differently, QD APDs on Si are not sensitive to dislocations and thus have the ideal dark current. However, the speed, responsivity, and excess noise performance are not comparable to bulk semiconductor APDs. More optimized APD structures should be adopted to improve the overall performance of QD APDs.

3. Conclusion

In conclusion, we reviewed recent advances of the integrated APDs on silicon. The APDs on SiPh can leverage rewards of high-performance optical receivers and CMOS-compatible SiPh-integrated circuits, therefore provide an attractive Rx solution with standard manufacturing processes and low costs. One great advantage of APDs over PDs is its intern-

al gain allows the optical links to have better SNR, which is crucial for many applications, such as future high-density, low-latency, and low-power optical interconnects. In past decades, numerous effort has been done to realize APDs on Si using monolithic or heterogeneous methods, and diverse semiconductor systems, including Si–Ge and III–V. Due to their great performance, especially the low excess noise and high sensitivity, integrated APDs will be of great use in a broad range of applications. It is not difficult to predict that high-quality APDs on Si will create a large market and become a powerful technology for explosive data growth.

References

[1] Piels M, Bowers J E. Photodetectors for silicon photonic integrated circuits. Photodetectors. Amsterdam: Elsevier, 2016, 3

[2] Fédéli J M, Virot L, Vivien L, et al. High-performance waveguide-integrated germanium PIN photodiodes for optical communication applications. 2014 7th Int Silicon Ger Technol Device Meet ISTDM, 2014, 131

[3] Virot L, Benedikovic D, Szelag B, et al. Integrated waveguide PIN photodiodes exploiting lateral Si/Ge/Si heterojunction. Opt Express, 2017, 25, 19487

[4] Sun K Y, Tzu T C, Costanzo R, et al. Ge-on-Si balanced periodic traveling-wave photodetector. 2019 IEEE Photonics Conference (IPC), 2019, 1

[5] Bogaert L, van Gasse K, Spuesens T, et al. Silicon photonics traveling wave photodiode with integrated star coupler for high-linearity mm-wave applications. Opt Express, 2018, 26, 34763

[6] Xie X J, Zhou Q G, Norberg E, et al. High-power and high-speed heterogeneously integrated waveguide-coupled photodiodes on silicon-on-insulator. J Lightwave Technol, 2016, 34, 73

[7] Muliuk G, Zhang J, Goyvaerts J, et al. High-yield parallel transfer print integration of III-V substrate-illuminated C-band photodiodes on silicon photonic integrated circuits. Proc SPIE 10923, Silicon Photonics XIV, 2019, 1092

[8] Sun K Y, Jung D, Shang C, et al. Low dark current III–V on silicon photodiodes by heteroepitaxy. Opt Express, 2018, 26, 13605

[9] Sun K Y, Gao J Y, Jung D, et al. 40 Gbit/s waveguide photodiode using III–V on silicon heteroepitaxy. Opt Lett, 2020, 45, 2954

[10] Casalino M, Iodice M, Sirleto L, et al. Asymmetric MSM sub-bandgap all-silicon photodetector with low dark current. Opt Express, 2013, 21, 28072

[11] Cansizoglu H, Mayet A S, Ghandiparsi S, et al. Dramatically enhanced efficiency in ultra-fast silicon MSM photodiodes via light trapping structures. IEEE Photonics Technol Lett, 2019, 31, 1619

[12] Akinwande D, Huyghebaert C, Wang C H, et al. Graphene and two-dimensional materials for silicon technology. Nature, 2019, 573, 507

[13] Gonzalez Marin J F, Unuchek D, Watanabe K, et al. MoS_2 photodetectors integrated with photonic circuits. npj 2D Mater Appl, 2019, 3, 1

[14] Campbell J C. Recent advances in avalanche photodiodes. J Lightwave Technol, 2016, 34, 278

[15] Benedikovic D, Virot L, Aubin G, et al. Silicon–germanium receivers for short-wave-infrared optoelectronics and communications. Nanophotonics, 2021, 10, 1059

[16] McIntyre R J. Multiplication noise in uniform avalanche diodes. IEEE Trans Electron Devices, 1966, ED-13,164

[17] Emmons R B. Avalanche-photodiode frequency response. J Appl Phys, 1967, 38, 3705

[18] Benedikovic D, Virot L, Aubin G, et al. 40 Gbps heterostructure germanium avalanche photo receiver on a silicon chip. Optica, 2020, 7, 775

[19] Srinivasan S A, Berciano M, de Heyn P, et al. 27 GHz silicon-contacted waveguide-coupled Ge/Si avalanche photodiode. J Lightwave Technol, 2020, 38, 3044

[20] Zhang J, Kuo B P P, Radic S. 64Gb/s PAM4 and 160Gb/s 16QAM modulation reception using a low-voltage Si-Ge waveguide-integrated APD. Opt Express, 2020, 28, 23266

[21] Zeng X G, Huang Z H, Wang B H, et al. Silicon–germanium avalanche photodiodes with direct control of electric field in charge multiplication region. Optica, 2019, 6, 772

[22] Huang Z H, Li C, Liang D, et al. 25 Gbps low-voltage waveguide Si–Ge avalanche photodiode. Optica, 2016, 3, 793

[23] Kang Y M, Liu H D, Morse M, et al. Monolithic germanium/silicon avalanche photodiodes with 340 GHz gain-bandwidth product. Nat Photonics, 2009, 3, 59

[24] Huang M Y, Cai P F, Li S, et al. 56GHz waveguide Ge/Si avalanche photodiode. Optical Fiber Communication Conference (OFC), 2018

[25] Li X W, Zheng X G, Wang S L, et al. Calculation of gain and noise with dead space for GaAs and $Al_xGa_{1-x}As$ avalanche photodiode. IEEE Trans Electron Devices, 2002, 49, 1112

[26] Rees G J, David J R. Nonlocal impact ionization and avalanche multiplication. J Phys D, 2010, 43, 243001

[27] Jamil E, Cheong J S, David J P, et al. On the analytical formulation of excess noise in avalanche photodiodes with dead space. Opt Express, 2016, 24, 21597

[28] Yuan Y, Huang Z H, Wang B H, et al. 64 Gbps PAM4 Si-Ge waveguide avalanche photodiodes with excellent temperature stability. J Lightwave Technol, 2020, 38, 4857

[29] Harrison C N, David J P R, Hopkinson M, et al. Temperature dependence of avalanche multiplication in submicron $Al_{0.6}Ga_{0.4}As$ diodes. J Appl Phys, 2002, 92, 7684

[30] Jones A H, Yuan Y, Ren M, et al. $Al_xIn_{1-x}As_ySb_{1-y}$ photodiodes with low avalanche breakdown temperature dependence. Opt Express, 2017, 25, 24340

[31] Yuan Y, Huang Z H, Wang B H, et al. Superior temperature performance of Si-Ge waveguide avalanche photodiodes at 64Gbps PAM4 operation. Optical Fiber Communication Conference (OFC) 2020, 2020

[32] Wang B H, Huang Z H, Yuan Y, et al. 64 Gb/s low-voltage waveguide SiGe avalanche photodiodes with distributed Bragg reflectors. Photon Res, 2020, 8, 1118

[33] Yuan Y, Huang Z H, Zeng X G, et al. High responsivity Si-Ge waveguide avalanche photodiodes enhanced by loop reflector. IEEE J Sel Top Quantum Electron, 2022, 28, 1

[34] Liu A Y, Bowers J. Photonic integration with epitaxial III–V on silicon. IEEE J Sel Top Quantum Electron, 2018, 24, 1

[35] Han Y, Xue Y, Yan Z, et al. Selectively grown III-V lasers for integrated Si-photonics. J Lightwave Technol, 2021, 39, 940

[36] Liang D, Bowers J E. Recent progress in heterogeneous III-V-on-silicon photonic integration. Light: Adv Manuf, 2021, 2, 1

[37] Li N, Sidhu R, Li X W, et al. InGaAs/InAlAs avalanche photodiode with undepleted absorber. Appl Phys Lett, 2003, 82, 2175

[38] Nada M, Yokoyama H, Muramoto Y, et al. A 50-Gbit/s vertical illumination avalanche photodiode for 400-Gbit/s Ethernet systems. Opt Express, 2014, 22, 14681

[39] Nada M, Nakamura M, Matsuzaki H. 25-Gbit/s burst-mode optical receiver using high-speed avalanche photodiode for 100-Gbit/s optical packet switching. Opt Express, 2014, 22, 443

[40] Zhao Y L, Zhang D D, Qin L, et al. InGaAs–InP avalanche photodiodes with dark current limited by generation-recombination. Opt Express, 2011, 19, 8546

[41] Meng X, Tan C H, Dimler S, et al. 1550 nm InGaAs/InAlAs single photon avalanche diode at room temperature. Opt Express,

2014, 22, 22608
[42] Liu M G, Hu C, Bai X G, et al. High-performance InGaAs/InP single-photon avalanche photodiode. IEEE J Sel Top Quantum Electron, 2007, 13, 887
[43] Ren M, Gu X R, Liang Y, et al. Laser ranging at 1550 nm with 1-GHz sine-wave gated InGaAs/InP APD single-photon detector. Opt Express, 2011, 19, 13497
[44] Liu X B, Li Li. Design of the optical system of flash lidar based on an APD array. Infrared Laser Eng, 2009, 38, 893
[45] Schwarz B. Mapping the world in 3D. Nat Photonics, 2010, 4, 429
[46] Adamo G, Busacca A. Time of flight measurements via two LiDAR systems with SiPM and APD. 2016 AEIT International Annual Conference (AEIT), 2016
[47] Elshaari A W, Pernice W, Srinivasan K, et al. Hybrid integrated quantum photonic circuits. Nat Photonics, 2020, 14, 285
[48] Moody G, Sorger V J, Juodawlkis P W, et al. Roadmap on integrated quantum photonics. arXiv preprint arXiv: 2102.03323, 2021
[49] Keyvaninia S, Muneeb M, Stanković S, et al. Ultra-thin DVS-BCB adhesive bonding of III-V wafers, dies and multiple dies to a patterned silicon-on-insulator substrate. Opt Mater Express, 2012, 3, 35
[50] Zhang J, Muliuk G, Juvert J, et al. III-V-on-Si photonic integrated circuits realized using micro-transfer-printing. APL Photonics, 2019, 4, 110803
[51] Lucci I, Charbonnier S, Pedesseau L, et al. Universal description of III-V/Si epitaxial growth processes. Phys Rev Materials, 2018, 2, 060401
[52] Yuan Y, Jung D, Sun K, et al. III-V on silicon avalanche photodiodes by heteroepitaxy. Opt Lett, 2019, 44, 3538
[53] Nakata T, Ishihara J, Makita K, et al. Multiplication noise characterization of InAlAs-APD with heterojunction. IEEE Photonics Technol Lett, 2009, 21, 1852
[54] Jutzi M, Berroth M, Wöhl G, et al. Zero biased Ge-on-Si photodetector on a thin buffer with a bandwidth of 3.2 GHz at 1300 nm. Mater Sci Semicond Process, 2005, 8, 423
[55] Colace L, Ferrara P, Assanto G, et al. Low dark-current germanium-on-silicon near-infrared detectors. IEEE Photonics Technol Lett, 2007, 19, 1813
[56] Tossoun B, Kurczvcil G, Zhang C, et al. High-speed 1310 nm hybrid silicon quantum dot photodiodes with ultra-low dark current. 2018 76th Device Research Conference (DRC), 2018, 1
[57] Fang A W, Park H, Jones R, et al. A continuous-wave hybrid AlGaInAs-silicon evanescent laser. IEEE Photon Technol Lett, 2006, 18, 1143
[58] Bowers J E. Evolution of photonic integrated circuits. 2017 75th Annual Device Research Conference (DRC), 2017, 1
[59] Tossoun B, Kurczveil G, Zhang C, et al. Indium arsenide quantum dot waveguide photodiodes heterogeneously integrated on silicon. Optica, 2019, 6, 1277
[60] Tossoun B, Srinivasan S, Descos A, et al. High-speed heterogeneous quantum dot avalanche photodiodes with polarization dependent gain. 2020 IEEE Photonics Conference (IPC), 2020, 1
[61] Tossoun B, Kurczveil G, Srinivasan S, et al. 32 Gbps heterogeneously integrated quantum dot waveguide avalanche photodiodes on silicon. Opt Lett, 2021, 46, 3821
[62] Ishikawa H, Shoji H, Nakata Y, et al. Self-organized quantum dots and quantum dot lasers. J Vac Sci Technol A, 1998, 16, 794
[63] Liang D, Bowers J E. Highly efficient vertical outgassing channels for low-temperature InP-to-silicon direct wafer bonding on the silicon-on-insulator substrate. J Vac Sci Technol B, 2008, 26, 1560
[64] Jin P, Li C M, Zhang Z Y, et al. Quantum-confined Stark effect and built-in dipole moment in self-assembled InAs/GaAs quantum dots. Appl Phys Lett, 2004, 85, 2791
[65] Umezawa T, Akahane K, Matsumoto A, et al. Polarization dependence of avalanche multiplication factor in 1.5 μm quantum dot waveguide photodetector. Conference on Lasers and Electro-Optics, 2016
[66] Wu J, Jiang Q, Chen S M, et al. Monolithically integrated InAs/GaAs quantum dot mid-infrared photodetectors on silicon substrates. ACS Photonics, 2016, 3, 749
[67] Sandall I, Ng J S, David J P R, et al. 1300 nm wavelength InAs quantum dot photodetector grown on silicon. Opt Express, 2012, 20, 10446
[68] Wan Y T, Zhang Z Y, Chao R L, et al. Monolithically integrated InAs/InGaAs quantum dot photodetectors on silicon substrates. Opt Express, 2017, 25, 27715
[69] Chen B L, Wan Y T, Xie Z Y, et al. Low dark current high gain InAs quantum dot avalanche photodiodes monolithically grown on Si. ACS Photonics, 2020, 7, 528
[70] Pauchard A, Bitter M, Sengupta D, et al. High-performance InGaAs-on-silicon avalanche photodiodes. Optical Fiber Communication Conference and Exhibit, 2002, 345
[71] Umezawa T, Akahane K, Kanno A, et al. Investigation of a 1.5-μm-wavelength InAs-quantum-dot absorption layer for high-speed photodetector. Appl Phys Express, 2014, 7, 032201

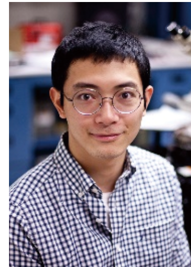

Yuan Yuan received the BS degree from Nanjing University of Aeronautics and Astronautics, Nanjing, China, in 2016 and a PhD degree from University of Virginia, Charlottesville, VA, USA, in 2019, both in electrical engineering. He is currently a Research Scientist with Hewlett Packard Labs of Hewlett Packard Enterprise (HPE), Milpitas, CA, USA. His research interests include avalanche photodiodes, single photon counting, III–V and silicon photonics. He is a member of IEEE and OSA.

Bassem Tossoun received his BS degree in Computer Engineering and MS degree in Electrical Engineering from Cal Poly San Luis Obispo in 2014. He completed his PhD in Electrical Engineering at the University of Virginia in 2019 with his research interests including silicon photonics and the design, fabrication, and characterization of optoelectronic devices. Currently, he is a Research Scientist at Hewlett Packard Labs working on quantum dot photodiodes and memristor photonics for next-generation supercomputers.

Zhihong Huang received a BS degree from Peking University, Beijing, China, and the MS and PhD degrees in electrical engineering from The University of Texas at Austin, Austin, TX, USA. She is a Research Scientist with Hewlett Packard Labs, leading the development of low power optical transceivers for optical interconnects. Her research topics include avalanche photodiodes, single photon counting, optical sensors, nano-photonics, silicon photonics, as well as quantum information processing. She has authored or coauthored more than 70 journal and conference papers, and was granted more than 20 US/international patents with another dozen pending.

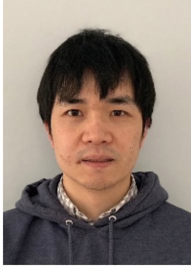

Xiaoge Zeng received a BSc degree in physics from the University of Science and Technology of China, Hefei, China, in 2008 and a PhD degree in physics from the University of Colorado Boulder, Boulder, CA, USA, in 2015. Since 2016, he has been a Research Scientist with the Hewlett Packard Labs, CA, USA. His research interests include silicon photonics, integrated optics, optical communications, nonlinear, and quantum optics.

Geza Kurczveil is a research scientist in HPE's Large-Scale Integrated Photonics Lab in Santa Barbara, California. He received his PhD degree in Electrical and Computer Engineering from the University of California, Santa Barbara in 2012 working on optical buffers. His current research interests include comb lasers, silicon photonic-integrated circuits, and nanophotonics. He has authored and co-authored over 50 journal and conference papers.

Marco Fiorentino received a PhD degree in physics from the University of Naples, Naples, Italy, in 2000. His doctoral work focused on quantum optics. He is a Research Scientist at the Large-Scale Integrated Photonics Lab, Hewlett Packard Enterprise Labs, Milpitas, CA, USA. Before working with the HP/HPE Labs, in 2005, he was with Northwestern University, the University of Rome, and MIT. In the past, he has worked on optics, high-precision measurements, and optical communications.

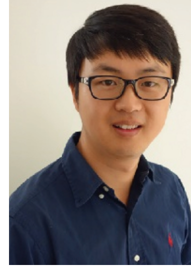

Di Liang is currently a Distinguished Technologist and Research Manager at Hewlett Packard Labs of Hewlett Packard Enterprise (HPE). His research interests include III–V and silicon photonics and heterogeneous material integration. He has authored and co-authored over 240 journal and conference papers, 7 book chapters, and was granted by 44 patents with another 55+ pending. He is a Fellow of OSA, a senior member of IEEE, and a member of SPIE.

Raymond G. Beausoleil received the B.S. degree from Caltech, Pasadena, CA, USA, in 1980, and a PhD degree from Stanford University, Stanford, CA, in 1986, both in physics. He is currently a Senior Fellow and Senior Vice President at Hewlett Packard Enterprise (HPE), San Jose, CA, where he is the Director of the Large-Scale Integrated Photonics Lab in Hewlett Packard Labs. Prior to HPE, his research was focused on high-power all- solid-state laser and nonlinear optical systems, as well as numerical algorithms for computer firmware (leading to the navigation algorithms for the optical mouse). At Hewlett Packard Labs, he performs basic and applied research in microscale and nanoscale classical and quantum optics for information processing technologies. He is an Adjunct Professor of Applied Physics at Stanford University, a Fellow of the American Physical Society and the Optical Society of America, and the recipient of the 2016 APS Distinguished Lectureship on the Applications of Physics.